



# Description of deep saturated excitation multiphoton microscopy for super-resolution imaging

GENEVIEVE VIGIL, YIDE ZHANG, AAMIR KHAN, AND SCOTT HOWARD\*

Department of Electrical Engineering, University of Notre Dame, 275 Fitzpatrick Hall, Notre Dame, Indiana 46556, USA

\*Corresponding author: showard@nd.edu

Received 21 November 2016; revised 16 May 2017; accepted 30 May 2017; posted 2 June 2017 (Doc. ID 281151); published 27 June 2017

Here we recount the standard two-level model that describes saturated excitation (SAX) in multiphoton microscopy (MPM), a new technique for super-resolution fluorescence microscopy in scattering tissue, which requires no special chemistry and only simple modifications to a commercial MPM microscope. We use the model to study conditions required for improvements in MPM SAX resolution and experimental implementation strategies. Simulation results find zeros, or nodes, in the frequency response, which generate highly irregular point-spread functions (PSFs), such as rings and ripples, that contain spatial frequency content  $>3\times$  larger than allowed by diffraction. These PSFs are a direct result of zeros in the frequency response of saturated fluorophores under specific excitation conditions. The impact on image quality is discussed using simulations of targets imaged with SAX PSFs. Further, we explore engineering sets of irregular PSFs by varying the excitation power and reconstructing super-resolution images from the set of captured images. © 2017 Optical Society of America

**OCIS codes:** (170.2520) Fluorescence microscopy; (100.6640) Superresolution; (190.0190) Nonlinear optics.

<https://doi.org/10.1364/JOSAA.34.001217>

## 1. INTRODUCTION

Super-resolution fluorescence microscopy is a powerful tool for studying functional biochemistry applications at subcellular and molecular scales [1–3]. While super-resolution fluorescence microscopy has enabled groundbreaking research, fundamental and technical challenges have generally limited use to specific *in vitro* applications in nonscattering tissue. Super-resolution microscopy based on localization (i.e., determining the probable object location using statistical inference) requires dyes with special chemical properties and fine control of dye concentration [4,5]. Such examples include photoactivated localization microscopy [6] and stochastic optical reconstruction microscopy [7]. Super-resolution can also be achieved using spatially non-uniform illumination in techniques such as stimulated emission depletion microscopy [1,8] or structured illumination (SIM) [2,3]. These methods commonly require additional complexity by adding laser sources and optical components [1,2,9]. Additionally, the performance of current super-resolution fluorescence microscopy is highly degraded in scattering samples, and, thus, has limited imaging depth to a few micrometers [10,11].

To achieve three-dimensional (3D) depth-resolved super-resolution fluorescence microscopy, a new technique has been demonstrated that images the effects of fluorescence

saturation within a diffraction-limited spot using multiphoton microscopy (MPM). MPM is a widely used diffraction-limited fluorescence microscopy technique capable of imaging tissue structure over a millimeter deep *in vivo* [12–14]. When the intensity of the MPM excitation light is large, fluorophores within the focal volume will saturate. This saturation first occurs only at the center of the focal volume and then increases in size as the power increases, leading to PSF broadening [15]. Since the frequency response of saturated fluorophores to intensity-modulated excitation light is different from that of unsaturated molecules, super-resolution can be achieved by imaging effects that are solely attributed to saturated molecules within the focal volume. This technique, known as saturated excitation (SAX) microscopy, has been demonstrated to improve resolution by a factor of  $\sqrt{2}$  beyond the diffraction limit [16]. No specialized dyes and minimal hardware modifications are needed to transform a conventional MPM into a SAX microscope. Therefore, by leveraging all the 3D imaging capabilities of MPM and controlling the saturation state, 3D super-resolution microscopy can be achieved.

Previous work has demonstrated SAX in the single-photon [17] and two-photon regimes [16,18]. However, when considering potential performance improvements and implementation strategies, theoretical models describing SAX have been

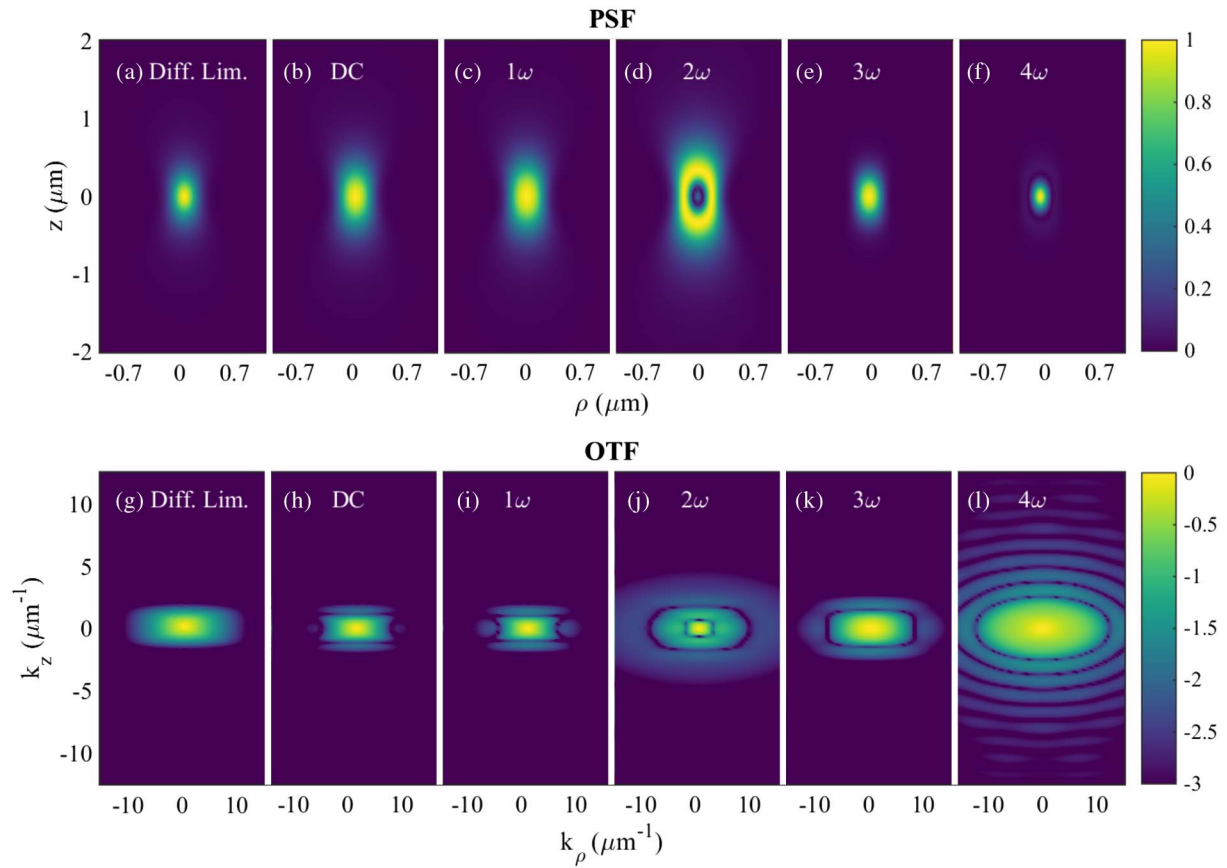


**Fig. 1.** Examples of [(a)–(f)] SAX PSFs and [(g)–(l)] OTFs using excitation powers of  $2\times$  the onset of saturation. The (a, g) diffraction-limited, (b, h) DC, (c, i)  $1\omega$ , (d, j)  $2\omega$ , (e, k)  $3\omega$ , (f, l) and  $4\omega$  cases are shown. Notice the saturation broadened DC (b) and  $1\omega$  (c) PSFs. Sub-diffraction PSFs are found in the (e)  $3\omega$  and (f)  $4\omega$ . High-spatial-frequency components can be seen in (j) the  $2\omega$  and (l) the  $4\omega$  case. OTFs are shown on a log scale color map.

truncated to a few terms in a Taylor expansion [16], which do not accurately capture the highly nonlinear behavior of SAX MPM found in deep saturation. To more accurately develop MPM SAX resolution estimates and implementation strategies, we solve a complete physical model of MPM SAX and analyze the resulting PSFs in the spatial frequency domain. The modeled PSFs do indeed show both small, Gaussian-like shapes as well as highly non-Gaussian PSFs containing high-spatial-frequency features within the PSF. These non-Gaussian PSFs have been demonstrated previously in SAX microscopy [19], and this work presents a theoretical basis of the phenomenon in order to better understand and use these for super-resolution imaging. These higher spatial frequency features arise from zeros in the emission harmonic magnitudes at specific excitation conditions. We refer to these regions as nodes throughout this text and will show how these nodes contribute to highly non-Gaussian and sub-diffraction PSFs such as those exemplified in Fig. 1, and, therefore, enable even higher resolution capabilities than predicted previously for SAX MPM [16].

## 2. TWO-LEVEL SYSTEM MODEL

The rate equation governing the excitation dynamics of a two-level system in which absorption, stimulated emission, and

spontaneous emission are the primary drivers of observed fluorescence can be written as a function of axial position ( $z$ ), lateral position ( $\rho$ ), and time ( $t$ ) as [15]

$$\frac{d\Delta N(\rho, z, t)}{dt} + (2W(\rho, z, t) + \gamma)\Delta N(\rho, z, t) = \gamma, \quad (1)$$

where  $\Delta N(\rho, z, t)$  is the population difference between the ground and excited states,  $W(\rho, z, t)$  is the rate of absorption and stimulated emission, and  $\gamma$  is the rate of spontaneous emission, which is related to fluorescence lifetime by  $\tau = 1/\gamma$ . A solution to a differential equation of this form can be written as

$$\Delta N(\rho, z, t) = \frac{\int \exp\left(\int 2W(\rho, z, t) + \gamma dt\right) dt}{\gamma \exp\left(\int 2W(\rho, z, t) + \gamma dt\right)}, \quad (2)$$

where  $W(\rho, z, t)$  is proportional to the two-photon absorption cross section,  $\sigma$ , and the spatial and temporal profiles of the excitation,  $S(x, y, z) = S(\rho, z)$  and  $A(t)$ , respectively. In the case where  $W(\rho, z, t)$  is many orders of magnitude faster than  $\gamma$ , Eq. (2) can be simplified to

$$\Delta N(\rho, z, t) = \gamma \exp\left[-2\sigma S(\rho, z)^2 \times \int A(t)^2 dt\right] \times \exp[-\gamma t] \int \exp[\gamma t] dt, \quad (3)$$

and further to

$$\Delta N(\rho, z, t) = \exp\left[-2\sigma S(\rho, z)^2 \int A(t)^2 dt\right]. \quad (4)$$

Depending on the specific temporal shape of the excitation pulse,  $A(t)$ , an analytical or numerical integration can be performed to arrive at the final form of  $\Delta N(\rho, z, t)$  after a single pulse. It should be noted that constants of integration have been set to unity expressing the assumption that all molecules excited by a given pulse relax back to the ground state prior to the subsequent laser pulse. The fluorescence will ultimately be proportional to the population of the excited state, and from a total population set to unity, the excited state probability can be found as

$$N_1(\rho, z, t) = \frac{1}{2}(1 - \Delta N(\rho, z, t)). \quad (5)$$

If the excitation is modulated by a periodic function  $F_m(t)$  with frequency  $\omega_m$  much slower than the pulse repetition rate, and can therefore be treated as a constant over the pulse integration, the overall excited state probability can be denoted as

$$N_1(\rho, z, t) = \frac{1}{2} \left( 1 - \exp\left[-2\sigma S(\rho)^2 \int A(t)^2 dt F_m(t)^2\right] \right). \quad (6)$$

In this work, we will consider the impact on imaging resolution for a sinusoidal modulation function of the form

$$F_m(t) = \frac{1}{2}(\cos(\omega_m t) + 1), \quad (7)$$

spatial beam profiles of the form

$$S(\rho, z) = \frac{2}{\pi w(z)^2} e^{-2\frac{\rho^2}{w(z)^2}}, \quad (8)$$

and temporal pulse profiles of the form

$$A(t) = \frac{2\langle P \rangle}{h\nu} \sqrt{\frac{\ln 2}{\pi}} \frac{1}{f_p \alpha} e^{-\ln 2 \left(\frac{2(t-t_0)}{\alpha}\right)^2}, \quad (9)$$

where  $w(z)^2 = \left(\frac{\lambda}{\pi \text{NA}}\right)^2 \left(1 + \left(\frac{z}{z_R}\right)^2\right)$ , NA is the numerical aperture of the objective,  $\lambda$  is the wavelength of excitation light,  $z_R = \lambda/\pi \text{NA}^2$ ,  $\langle P \rangle$  is the average optical power,  $f_p$  is the pulse repetition rate, and  $\alpha$  is the pulse width. Inserting Eqs. (7)–(9) into Eq. (6), an expression for the excited state probability can be simplified to

$$N_1 = \frac{1}{2} \left( 1 - e^{-\left(\frac{1}{2}\cos(\omega t) + \frac{1}{2}\right)^2 2\sigma S(\rho, z)^2 \beta} \right), \quad (10)$$

where  $\beta(t) = \frac{8 \ln 2}{\sqrt{\pi \alpha}} \left(\frac{\langle P \rangle}{h\nu f_p}\right)^2$ . Even in the unsaturated case, the fluorescence signal will have the frequency characteristics of  $(1/2 \cos(\omega t) + 1/2)^2 = 1/2 \cos(\omega t) + 1/8 \cos(2\omega t) + 3/8$ , and, thus, both the first and second harmonics should exist. In the saturated case, the crests of the squared sinusoid flatten out and higher order harmonic terms are present in the spectrum.

These higher order terms can be found numerically by simulating Eq. (10) for specific experimental conditions.

### 3. SIMULATION AND PRELIMINARY RESULTS

Equation (6) was solved numerically with a sinusoidally varying excitation amplitude in Eq. (7) and with simulation parameters  $\sigma = 150$  GM, NA = 0.8, and  $\lambda = 800$  nm. PSFs corresponding to the magnitude of each harmonic component were reconstructed from the Fourier transform of  $N_1(\rho, z, t)$ . Simulation work was performed in MATLAB (Mathworks, Natick, MA) by solving for the excited state population density PSF,  $N_1(\rho, z, t)$ , after every pulse over a time of several modulation periods with a spatial grid size of  $2 \times 10^{-2}$  times the diffraction-limited beam waist. In the numerical simulation,  $N_1$  is solved in a series of nested loops for every point in  $z$  and  $\rho$  and for a given pulse occurring at time  $t$ . This computation is performed for every  $t$  over several modulation cycles.  $N_1$  is therefore a 3D matrix (radial, axial, and temporal) on which Fourier transforms are performed along the time dimension. Every point in space then has an associated frequency spectrum from which harmonics are selected by indexing. Each PSF associated with a particular harmonic is mapped out in real space before a spatial Fourier transform is performed to analyze the spatial frequency content of the optical transfer function (OTF) contained in each harmonic PSF. The numerical modeling source code is available for use and inspection [20]. Example PSFs and OTFs are presented in Fig. 1 for several MPM SAX harmonic frequencies when the saturation depth is 2. The physical origin of these PSFs and their application to super-resolution imaging are presented below. Additionally, the set of computed MPM SAX PSFs and OTFs versus saturation depth is provided as [Visualization 1](#). An experimental demonstration was performed using the microscope setup explained in [21]. Fluorescence from a single point focused on a cuvette of Rhodamine B in water was measured and harmonic components were extracted by Fourier analysis.

The calculated response for a single fluorophore located at the center of the diffraction PSF is shown in Fig. 2 along with a preliminary demonstration of fluorescence nodes measured in deep saturation. Saturation depth is defined as the average excitation power,  $\langle P \rangle$ , divided by the power at which emission reaches 1/2 the saturated value,  $\langle P_{\text{sat}} \rangle$ . As expected, the magnitude of the DC component before saturation increases with power squared, as expected in two-photon emission. Saturation is clearly seen when the DC component (blue solid line) departs from the ideal, two-photon behavior (black dashed line), as predicted from the steady-state solution of Eq. (1). Local saturation is seen to occur at relatively shallow saturation depths. Node behavior is confirmed experimentally in fluorescence measurements optimized for deep saturation; i.e., due to the limited dynamic range of the photon multiplying tube (PMT), the high-power regime was optimized, resulting in a poor signal-to-noise ratio (SNR) in the low-power range.

The magnitudes of the higher harmonics attributed to saturation ( $\geq 3\omega$ ) increase faster than power squared and exhibit discontinuities in slope at specific saturation depths. The frequency response is a complex function and at low modulation frequencies, the signal is nearly entirely real and therefore

sufficiently described in magnitude plots here. However, the harmonic signal on either side of the node will be  $\pi$  out of phase from itself (i.e., negative) [19]. Therefore, the resulting PSF is complex in addition to being non-Gaussian and, therefore, the phase and magnitude of the PSF must be accounted for in the resulting image deconvolution. The existence of such nodes contributes two interesting results, which, combined, produce a PSF with a higher spatial resolution than allowed by diffraction: (1) the increase in harmonic magnitude grows faster than  $P^2$  near nodes and (2) the nodes create zeros in the PSF. For example, the local excitation at the center of a PSF could be such that little to no second harmonic component is found. This would result in a ring-like PSF in the second harmonic, which is shown in Fig. 1(d).

The super-resolution capability of SAX MPM is established by analyzing the resulting PSFs in the spatial frequency domain. Imaging is the convolution of a PSF with an object ( $i(\vec{r}) = h(\vec{r}) \otimes o(\vec{r})$ ), which corresponds to a multiplication in the spatial frequency domain ( $I(\vec{k}) = H(\vec{k}) \times O(\vec{k})$ ). The spatial frequency components of the PSF, known as the OTF [ $H(\vec{k})$ ], therefore act as a spatial frequency filter. In order to image small, high-spatial-frequency features in an object, the

OTF must contain those spatial frequencies. Super-resolution OTFs have higher spatial frequencies than are present in diffraction-limited OTFs. This is demonstrated in Fig. 1 where the OTFs for the generated SAX PSFs are compared to the diffraction-limited OTF at a saturation depth of 2.

To illustrate the performance of MPM SAX generally, the log magnitudes of the axial and lateral spectral frequency components are shown versus saturation depth in Fig. 3. At low saturation depth, the DC ( $0\omega$ ) OTF contains the spatial frequencies corresponding to a diffraction-limited spot. When saturation depth increases, the spatial frequency content in the DC component decreases as expected due to PSF broadening [15]. However, increase of saturation depth creates spatial frequency content in the higher order SAX OTFs ( $\geq 2\omega$ ) that exceeds that available in the diffraction-limited case by a factor of  $>3$ . We can therefore obtain super-resolution by imaging a sample with several PSFs, each containing different super-resolution spatial frequency content, and then combine the resulting images using standard reconstruction techniques [22,23].

Another measure of optical resolution is the full width at half-maximum (FWHM) of the PSF. A comparison of

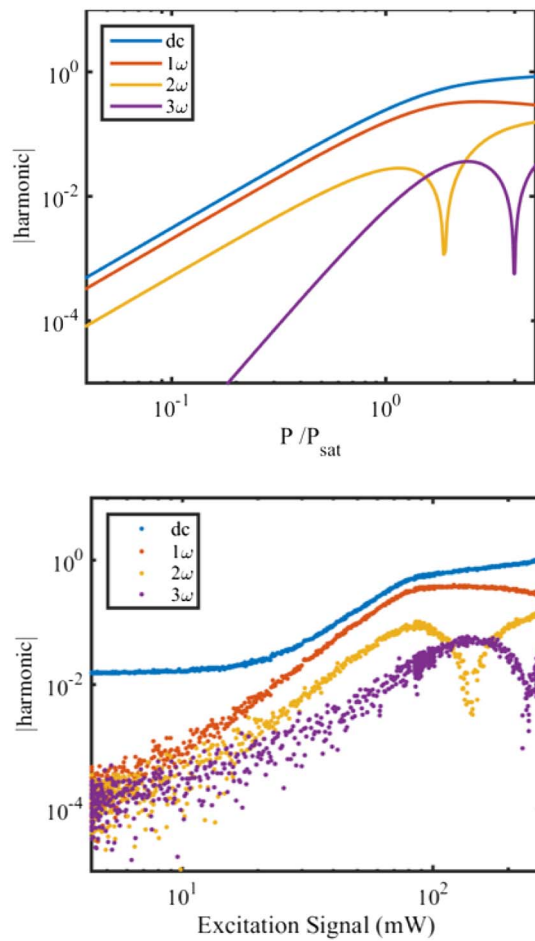


**Fig. 2.** Simulated harmonic magnitude at a single point in the excitation PSF with increasing saturation depth (top) and preliminary measured fluorescence experimental results (bottom). Node existence is predicted and confirmed in single point measurement.

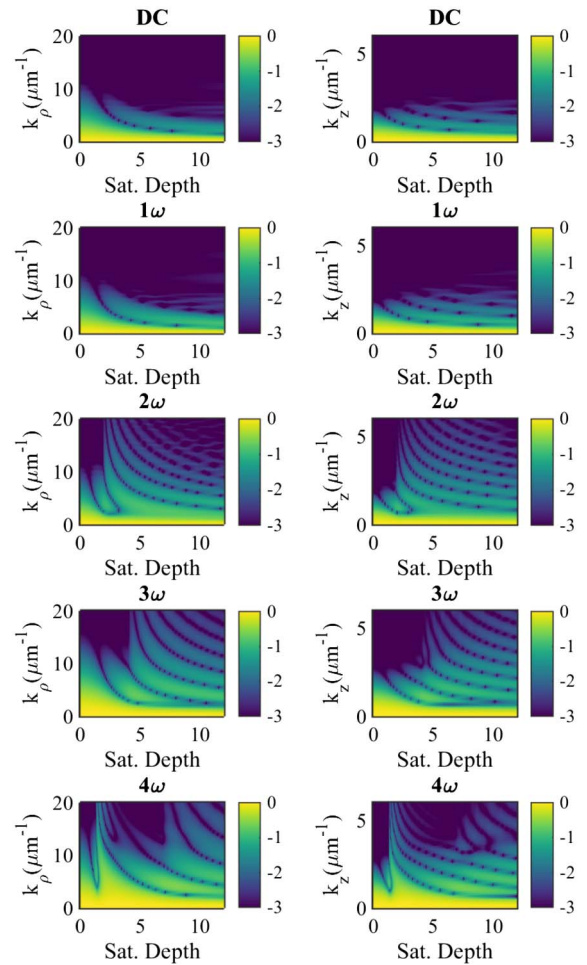


**Fig. 3.** Spatial frequency content of SAX generated PSFs in inverse radial (left) and axial (right) space across saturation depth. Diffraction limited results are equivalent to the DC spectrum at low (near 0) saturation depths. Shown on a log scale color map.

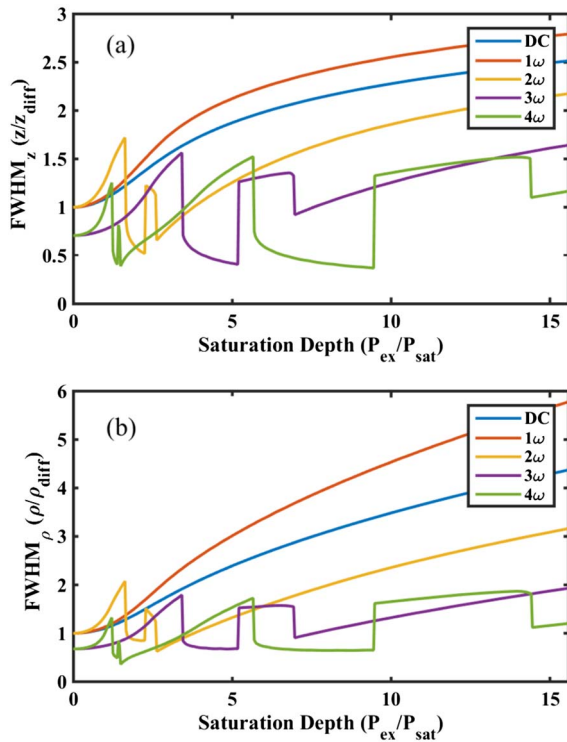


**Fig. 4.** FWHM of SAX PSFs with saturation depth. Harmonic PSFs can improve image resolution by a factor of  $>2\times$  over the diffraction limited case in both (a) the axial and (b) the radial direction.

the FWHM of the MPM SAX PSF is presented in Fig. 4 as a function of saturation depth. Since many of the PSFs are highly non-Gaussian, measures of FWHM do not describe the optical resolution performance as completely as the previous discussion of MPM SAX OTFs. Nonetheless, this compact figure allows a direct comparison to the diffraction-limited FWHM in a compact form. It can be seen that the FWHMs of saturation PSFs exhibit discontinuities resulting from nodes in the PSF. Even at a shallow depth of modulation, sub-diffraction resolution is possible for PSFs corresponding to harmonics  $\geq 3$ , whereas unmodulated (DC) MPM exhibits PSF broadening even at a low depth of modulation. Further, it can be seen that super-resolution PSFs can be generated in all harmonics at specific excitation conditions.

#### 4. DISCUSSION

In this section, simulation results will be discussed. The effects of SAX PSFs on image quality will be presented. Finally, the potential challenges and limitations related to SAX MPM will be examined.

Simulation results show that SAX MPM is capable of generating sub-diffraction PSFs compatible with 3D fluorescence imaging. The log-scale plots in Fig. 2 show a fluorophore’s optical response to intensity-modulated light. Two-photon emission is limited to a slope of 2 on this log-log plot. However, when saturated, the slope of the optical response can be greater than 2. In these cases, fluorophores at the center of a focal volume will respond to the excitation light more than fluorophores

on the periphery of the focal volume. The contrast between these two molecules inside the diffraction-limited PSF is greater than that in present in MPM, thus allowing super-resolution. Therefore, a slope of 2 on this log-log scale corresponds to the theoretical maximum of unsaturated two-photon emission and slopes greater than 2 indicate conditions of super-resolution. This illustrates one potential MPM SAX super-resolution strategy: image higher harmonic PSFs ( $\geq 3$ ) at the onset of saturation FWHMs are smaller than those in the diffraction-limited case and remain Gaussian-like in shape as done [16–18].

Additionally, super-resolution can be achieved even further by imaging the object with several high-spatial-frequency non-Gaussian PSFs. To illustrate this effect, Fig. 5 shows imaging with MPM SAX PSFs, of a resolution target containing variable-spatial-frequency components. The target is convolved with, i.e., imaged by, SAX-generated PSFs reconstructed from the Fourier analysis of an acquired time signal and corresponds to a saturation depth of 2. Notice that in this case, the DC and fundamental frequency images are already highly distorted over the diffraction-limited case. Additionally, the  $3\omega$  and  $4\omega$  show superior performance over the diffraction-limited case and uniformly resolve the target. In contrast, the  $2\omega$  component resolves the target non-uniformly and achieves super-resolution for features of a particular size. Therefore, scanning saturation depth allows imaging the same object with different spatial frequencies, thereby resolving the sizes of different features with each image. This is demonstrated in Visualization 2. A super-resolution image can then be reconstructed simply by using reconstruction methods including Wiener filter deconvolution [22] and maximum *a posteriori* estimation [23]. This method can be compared and contrasted with SIM methods in that both utilize irregular structures to observe high-spatial-frequency content. However, SIM methods introduce spatial frequencies that are outside of the normal resolving range into a detectable range through the use of resolvable interference patterns. SAX, however, directly excites a frequency response in a sub-diffraction-limited region, which can then be analyzed in the frequency domain. Another point of contrast is the time requirement for SAX- versus SIM-based methods. SIM uses wide-field illumination and imaging to acquire interference patterns rapidly, whereas SAX requires longer integration times in order to acquire the weaker saturation harmonics with adequate SNR for each pixel/voxel. This brings us to the trade-off between the two methods, SIM being fast but limited to imaging micrometer-scale depths, and SAX being capable of penetrating deeper into scattering tissue, but requiring more time. Additionally, the depth of penetration of SAX MPM should at least be comparable to that of other two-photon super-resolution techniques such as those in [24,25], since SAX MPM shares all the benefits of MPM. Additionally, SAX may even improve the penetration depth. Out-of-focus fluorescence near the surface of a scattering sample is the current limit for MPM [14]; however, saturation harmonics would not be present in this out-of-focus signal until greater powers or depths. It should also be noted that SAX presents a notable reduction in hardware complexity since super-resolution information is obtained primarily by post-processing as opposed to the addition of beam shaping/multiplexing optics.

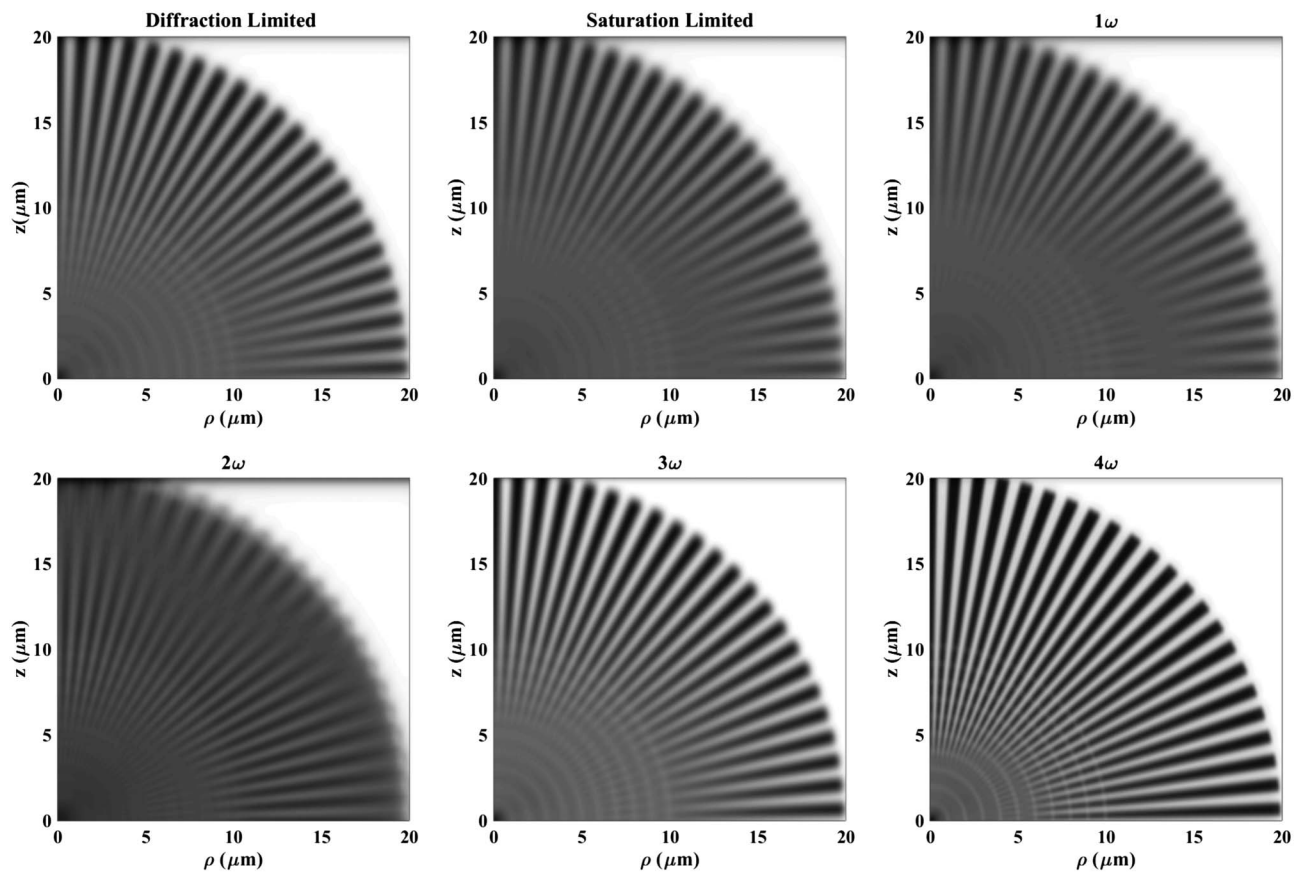


**Fig. 5.** Example of resolution targets imaged by simulated SAX PSFs. PSFs correspond to those shown in Fig. 1. Notice that finer details are available in the  $3\omega$  and  $4\omega$  cases compared to the diffraction limited case uniformly across the target of varying spatial frequency. In contrast, the blurring in the  $2\omega$  case is highly non-uniform, achieving super-resolution imaging only for specific spatial frequencies.

We have reported here an alternative method to perform super-resolution fluorescence imaging by using deep saturation SAX; however, a number of limitation and features must be considered further. Since this phenomenon is governed by highly nonlinear processes, accurate determination of excitation conditions which may produce favorable PSFs presents a unique challenge for SAX MPM. Further, since higher harmonic signals are significantly weaker than the initial intensity of the static emission, useful implementation of SAX MPM requires longer integration times than typical MPM ranging from several microseconds to milliseconds. Additionally, the power requirements to observe harmonics with sufficient SNRs require exposure dosages of the order of  $2\text{--}3\times$  that are required for typical MPM and comparable to those used in other *in vivo* fluoresce lifetime imaging [26]. In such applications, photobleaching has not been found to interfere with imaging capabilities. With careful design constraints kept in mind, SAX MPM may be optimized for various 3D fluorescence imaging in scattering tissue and adapted for *in vivo* applications.

## 5. CONCLUSION

A model describing saturation behavior and modulated SAX MPM based on a two-level electron system was recounted here. Based on this model, numerical calculations were performed

and we found that SAX MPM results in the potential to generate both super-resolved PSFs as well as irregular PSF geometries that contain high-spatial-frequency information. These results were analyzed for potential impact on imaging quality and found to produce interesting ability to resolve sub-diffraction features as well as features in a range of sizes depending only on excitation conditions such as laser power excitation and modulation form. Therefore, SAX provides a form of microscopy with tunable resolving power and potential for full super-resolution imaging using multi-image reconstruction algorithms. Careful experimental constraints and optimization will allow SAX MPM to be implemented as a super-resolution, 3D, fluorescence imaging tool for *in vivo* applications.

**Funding.** National Science Foundation (NSF) (CBET-1554516).

## REFERENCES

1. S. W. Hell, S. J. Sahl, M. Bates, X. Zhuang, R. Heintzmann, M. J. Booth, J. Bewersdorf, G. Shtengel, H. Hess, P. Tinnefeld, A. Honigsmann, S. Jakobs, I. Testa, L. Cognet, B. Lounis, H. Ewers, S. J. Davis, C. Eggeling, D. Klenerman, K. I. Willig, G. Vicidomini, M. Castello, A. Diaspro, and T. Cordes, "The 2015 super-resolution microscopy roadmap," *J. Phys. D* **48**, 443001 (2015).

2. B. O. Leung and K. C. Chou, "Review of super-resolution fluorescence microscopy for biology," *Appl. Spectrosc.* **65**, 967–980 (2011).
3. R. Heintzmann and M. G. L. Gustafsson, "Subdiffraction resolution in continuous samples," *Nat. Photonics* **3**, 362–364 (2009).
4. B. Huang, M. Bates, and X. Zhuang, "Super resolution fluorescence microscopy," *Annu. Rev. Biochem.* **78**, 993–1016 (2010).
5. E. Betzig, "Proposed method for molecular optical imaging," *Opt. Lett.* **20**, 237–239 (1995).
6. E. Betzig, G. H. Patterson, R. Sougrat, O. W. Lindwasser, S. Olenych, J. S. Bonifacino, M. W. Davidson, J. Lippincott-Schwartz, and H. F. Hess, "Imaging intracellular fluorescent proteins at nanometer resolution," *Science* **313**, 1642–1645 (2006).
7. B. Huang, W. Wang, M. Bates, and X. Zhuang, "Three-dimensional super-resolution imaging by stochastic optical reconstruction microscopy," *Science* **319**, 810–813 (2008).
8. S. W. Hell and J. Wichmann, "Breaking the diffraction resolution limit by stimulated emission: stimulated-emission-depletion fluorescence microscopy," *Opt. Lett.* **19**, 780–782 (1994).
9. E. Betzig, S. W. Hell, and W. E. Moerner, "How the optical microscope became a nanoscope" (2014), pp. 1–7.
10. S. R. P. Pavani, M. A. Thompson, J. S. Biteen, S. J. Lord, N. Liu, R. J. Twieg, R. Piestun, and W. E. Moerner, "Three-dimensional, single-molecule fluorescence imaging beyond the diffraction limit by using a double-helix point spread function," *Proc. Natl. Acad. Sci. USA* **106**, 2995–2999 (2009).
11. G. Shtengel, J. A. Galbraith, C. G. Galbraith, J. Lippincott-Schwartz, J. M. Gillette, S. Manley, R. Sougrat, C. M. Waterman, P. Kanchanawong, M. W. Davidson, R. D. Fetter, and H. F. Hess, "Interferometric fluorescent super-resolution microscopy resolves 3D cellular ultrastructure," *Proc. Natl. Acad. Sci. USA* **106**, 3125–3130 (2009).
12. N. G. Horton, K. Wang, D. Kobat, C. G. Clark, F. W. Wise, C. B. Schaffer, and C. Xu, "*In vivo* three-photon microscopy of subcortical structures within an intact mouse brain," *Nat. Photonics* **7**, 205–209 (2013).
13. D. Kobat, M. E. Durst, N. Nishimura, A. W. Wong, C. B. Schaffer, and C. Xu, "Deep tissue multiphoton microscopy using longer wavelength excitation," *Opt. Express* **17**, 13354–13364 (2009).
14. P. Theer and W. Denk, "On the fundamental imaging-depth limit in two-photon microscopy," *J. Opt. Soc. Am. A* **23**, 3139–3149 (2006).
15. G. C. Cianci, J. Wu, and K. M. Berland, "Saturation modified point spread functions in two-photon microscopy," *Microsc. Res. Tech.* **64**, 135–141 (2004).
16. A. D. Nguyen, F. Duport, A. Bouwens, F. Vanholsbeeck, D. Egrise, G. Van Simaey, P. Emplit, S. Goldman, and S.-P. Gorza, "3D super-resolved *in vitro* multiphoton microscopy by saturation of excitation," *Opt. Express* **23**, 22667–22675 (2015).
17. K. Fujita, M. Kobayashi, S. Kawano, M. Yamanaka, and S. Kawata, "High-resolution confocal microscopy by saturated excitation of fluorescence," *Phys. Rev. Lett.* **99**, 1–4 (2007).
18. M. Yamanaka, S. Kawano, K. Fujita, N. I. Smith, and S. Kawata, "Beyond the diffraction-limit biological imaging by saturated excitation microscopy," *J. Biomed. Opt.* **13**, 050507 (2015).
19. H. Lee, R. Oketani, Y.-T. Huang, K.-Y. Li, Y. Yonemaru, M. Yamanaka, S. Kawata, K. Fujita, and S.-W. Chu, "Point spread function analysis with saturable and reverse saturable scattering," *Opt. Express* **22**, 26016–26022 (2014).
20. G. D. Vigil, "Effective PSF in Saturation Compute" (2015), doi: 10.7274/R04X55RC, <https://curate.nd.edu/show/sn009w05p71>.
21. Y. Zhang, A. A. Khan, G. D. Vigil, and S. S. Howard, "Investigation of signal-to-noise ratio in frequency-domain multiphoton fluorescence lifetime imaging microscopy," *J. Opt. Soc. Am. A* **33**, B1–B11 (2016).
22. L. P. Yaroslavsky and H. J. Caulfield, "Deconvolution of multiple images of the same object," *Appl. Opt.* **33**, 2157–2162 (1994).
23. M. G. L. Gustafsson, L. Shao, P. M. Carlton, C. J. R. Wang, I. N. Golubovskaya, W. Z. Cande, D. A. Agard, and J. W. Sedat, "Three-dimensional resolution doubling in wide-field fluorescence microscopy by structured illumination," *Biophys. J.* **94**, 4957–4970 (2008).
24. V. Andresen, K. Pollok, J.-L. Rinnenthal, L. Oehme, R. Günther, H. Spiecker, H. Radbruch, J. Gerhard, A. Sporbert, Z. Cseresnyes, A. E. Hauser, and R. Niesner, "High-resolution intravital microscopy," *PLoS One* **101**, 1435–1439 (2012).
25. P. W. Winter, A. G. York, D. D. Nogare, M. Ingaramo, R. Christensen, A. Chitnis, G. H. Patterson, and H. Shroff, "Two-photon instant structured illumination microscopy improves the depth penetration of super-resolution imaging in thick scattering samples," *Optica* **1**, 181–191 (2014).
26. S. S. Howard, A. Straub, N. G. Horton, D. Kobat, and C. Xu, "Frequency-multiplexed *in vivo* multiphoton phosphorescence lifetime microscopy," *Nat. Photon. Lett.* **7**, 33–37 (2012).